Article type: Full paper

Nanoscale elastic changes in two-dimensional $Ti_3C_2T_x$ (MXene) pseudocapacitive electrodes

Jeremy Come, Yu Xie, Michael Naguib, Stephen Jesse, Sergei V. Kalinin, Yury Gogotsi, Paul R. C. Kent, and Nina Balke**

Dr. J. Come, Dr. Y. Xie, Dr. S. Jesse, Dr. S. V. Kalinin, Dr. P. R. C. Kent, Dr. N. Balke

Center for Nanophase Materials Sciences, Oak Ridge National Laboratory, P.O. Box 2008, Oak Ridge, TN 37831, USA

E-mail: xiey@ornl.gov, balken@ornl.gov

Dr. P. R. C. Kent

Computer Science and Mathematics Division, Oak Ridge National Laboratory, P. O. Box 2008, Oak Ridge, TN 37831, USA

Dr. M. Naguib

Materials Science and Technology Division, Oak Ridge National Laboratory, Oak Ridge, TN 37831, USA

Prof. Y. Gogotsi

Department of Materials Science and Engineering & A.J. Drexel Nanomaterials Institute, Drexel University, Philadelphia, PA 19104, USA

Keywords: MXene, cation intercalation, elastic modulus, contact resonance atomic force microscopy

Abstract:

Designing sustainable electrodes for next generation energy storage devices relies on the understanding of their fundamental properties at the nanoscale, including the comprehension of ions insertion into the electrode and their interactions with the active material. One consequence

of ion storage is the change in the electrode volume resulting in mechanical strain and stress that can strongly affect the cycle life. Therefore, it is important to understand the changes of dimensions and mechanical properties occurring during electrochemical reactions. While the characterization of mechanical properties via macroscopic measurements is well documented, in-situ characterization of their evolution has never been achieved at the nanoscale. Here we report on in-situ imaging, combined with density functional theory of the elastic changes, of a two-dimensional (2D) titanium carbide ($Ti_3C_2T_x$) based electrode in direction normal to the basal plane (electrode surface) during alkaline cation intercalation/extraction. 2D carbides, known as MXenes, are promising new materials for supercapacitors and various kinds of batteries, and understating the coupling between their mechanical and electrochemical properties is therefore necessary. The results show a strong correlation between the cations content and the out-of-plane elastic modulus. This strategy enables identifying the preferential intercalation pathways within a single particle, which is important for understanding ionic transport in these materials.

1. Introduction

The anisotropy of 2D compounds is responsible for their unique optical,[1] electronic,[2] or electrochemical properties.[3] While graphene is undoubtedly the most studied material, MoS_2,[4] graphene oxide,[5] boron nitride,[6] and other 2D materials show great promise and are being widely studied. Elasticity is certainly one of the most interesting properties of 2D and layered materials because it relies on a high anisotropy between their different crystallographic orientations. The in-plane elasticity of 2D materials has been extensively studied, and the Young's modulus can reach 1 TPa in the case of single-layer graphene,[7] whereas the out-of-plane modulus of multilayer graphene is only ~40 GPa.[8] While in-plane elasticity is an intrinsic property of 2D compounds, the out-of-plane counterpart depends on the number of layers and can be tuned to cater to specific requirements. Characterizing the normal-to-the-plane elastic modulus $E_{\perp}$ is essential for both fundamental understanding and for practical applications since it is related to thermal, electronic, tribological, and optical properties. To date, however, little is known about $E_{\perp}$ and only few experimental investigations have been reported for 2D materials because the measurements remain challenging. Even though it is now possible to probe the elasticity in the sub-nanometer surface layer,[9] most materials are polycrystalline and hold large ranges in the elasticity values.[10] Therefore, rather than single point characterization, imaging the mechanical properties throughout selected areas can provide helpful information on the intrinsic characteristics of the material. This is particularly interesting for energy materials, where the charge storage mechanism occurs preferentially on thermodynamically favorable sites with a low energy barrier.

It is well accepted that the stress generated by the electrochemical operation of energy storage materials contributes to the loss in the electrode mechanical integrity that is responsible for poor

electronic and ionic percolations, leading to increased internal resistance and performance loss. To date, in-situ strain measurements have been carried out on polyvinylidene fluoride polymer,[11] graphene oxide,[12] porous carbon,[13-15] or Li alloy electrodes,[16] however the elastic properties of the active materials associated with the electrochemical reactions have not been quantified so far.

Since recently, 2D transition metal carbides and carbonitrides (called MXenes) can easily be produced by selective etching of their parent layered MAX phase.[17-19] In these compounds, M is a transition metal atom, A is an atom from groups 3 or 5, and X is either C or N. Different approaches have been carried out to produce MX layers, and more than a dozen phases have been reported to date.[20,21] Their compositional versatility significantly broadened the spectrum of 2D materials and therefore opened exciting opportunities for various applications.[22-25] For example, it was predicted that the out-of-plane Young's modulus of a single Ti_3C_2 layer can exceed that of graphene,[26] and its in-plane elasticity has been predicted to be as high as 0.5 TPa.[27] However, no experimental measurements of mechanical properties of MXenes at the microscale have been reported so far. Thanks to their high electronic conductivity and hydrophilicity, MXenes have shown great promise for energy storage.[28,29] They particularly attracted attention due to extremely large and stable volumetric capacitance values (> 900 F cm^{-3} was achieved in H_2SO_4 electrolyte over 10,000 cycles),[30] associated with fast and reversible redox reaction of the surface Ti atoms in aqueous electrolytes.[30-32] Additionally, 2D $Ti_3C_2T_x$ (where T_x stands for the surface termination groups such as OH, O and F) exhibits large volume contraction during alkaline cation intercalation in aqueous electrolytes (up to 15% in the case of Li^+) that makes it attractive for electromechanical actuators.[33,34]

The quantification of mechanical properties for energy storage materials at the nanoscale lacks in-situ experimental technique that can be routinely used. Atomic Force Microscopy (AFM) has become a key tool to provide nanoscale morphology and mechanical properties with a high lateral resolution.[35,36] The mechanical properties can be extracted by analyzing the tip-sample contact interactions with mathematical models.[37-39] In particular, the vibrational modes of the AFM cantilever in contact with the surface are strongly dependent on the local elastic modulus of the sample. As a result, contact resonance (CR) frequency imaging has emerged as a powerful AFM technique for quantitative characterization of the elastic response of the materials with the advantage of providing this information quickly and with high resolution.[10,40] To date, contact resonance techniques were mostly limited to air environment because of complex cantilever dynamics models in liquids. However, recent developments in cantilever excitation avoiding traditional piezo drive signals have enabled more stable and reliable data acquisition in water.[41,42]

The goal of this study was to understand the coupling between electrochemical behavior and mechanical properties of electrodes made of 2D materials, by achieving a spatially-resolved characterization of cation intercalation. Here, the elastic properties of a $Ti_3C_2T_x$ electrode in the direction normal-to-the-basal plane during electrochemical intercalation/extraction of Li^+ and K^+ ions are quantified and imaged for the first time. These results provide a basis for in-situ mechanical characterizations of layered materials and intercalation compounds, as well as a fundamental understanding of the interplay between intercalated cations and the mechanics of 2D MXene sheets.

2. Results and Discussion

2.1. Quantification of mechanical properties using Contact Resonance AFM

Figure 1a represents the CR-AFM experimental setup used for tracking the resonance frequency as function of position and state of charge using the band excitation technique to quickly measure contact resonance cantilever dynamics while scanning.[43] The cantilever response to the multifrequency photothermal excitation was detected and Fourier transformed to identify the CR frequency at every point of the scan. The mechanics of the AFM tip-sample contact gives the connection between the experimentally measured values and the sample mechanical properties such as Young's modulus. The most commonly used model is the Hertz contact model (Figure 1b), where a spherical indenter with a radius r contacting a flat surface with a normal force F_N forms a contact radius a given by

$$a = \sqrt[3]{3F_N r/4E^*}, \quad (1)$$

where E^* is the reduced Young's modulus. For a defined cantilever oscillating in contact with a surface, its resonance frequency scales with the tip-sample contact stiffness k^* according to the model developed by Rabe [44] (see Supplementary Information 2 and 3 for more details). It is then possible to solve these models numerically and determine the frequency dependence as a function of k^*. For the AFM cantilever used in this study, the corresponding curve is shown in Figure 1c together with the measured resonance frequencies for two calibration samples: highly oriented pyrolytic graphite (HOPG) and fused silica. Then, as the cantilever scans over the surface, changes in the CR frequency provide a map of the localized stiffness. Because accurate determination of the contact area is extremely difficult, the acoustic AFM methods use an alternative approach involving a reference material (*ref*) with known properties (here, HOPG and

fused silica). The reduced modulus of the unknown sample (*s*) is then extracted in terms of the reference sample as:

$$E_S'^* = E_{ref}'^* \left(\frac{k_S^*}{k_{ref}^*}\right)^m , \quad (2)$$

where *m* is a constant that depends on the tip-sample geometry (*m* = 1.5 for a spherical contact, *m* = 1 for a flat punch). Note that this approach is only valid if the contact radius is the same on the unknown and reference samples. In order to minimize the role of local topography of the rough MXene electrode, flat particles were identified and investigated.

Although the above model is well-established in air and vacuum environments, the cantilever dynamics in liquids are still poorly characterized. It was evidenced to some extent that the frequency response dependence is very similar in both air and water, and that CR-AFM techniques are able to accurately measure the elastic and viscoelastic properties of solid materials immersed in liquids.[45,46] In order to validate the reliability of the measurements and achieve quantitative mechanical interpretation in liquid environment, we performed a series of calibrations in air and DI water using various samples with known elastic moduli (Supplementary Information 4). We applied the same mathematical formalism in water and in air, despite the different cantilever dynamics and the negligence of effects such as viscosity, turbulences, temperature gradients, etc. CR-AFM measurements were performed on MXene paper in air and DI water environments prior to any intercalation. The CR frequency distribution within a relatively flat $Ti_3C_2T_x$ flake was in the range of 245-270 kHz and 105-117 kHz in air and water, respectively (**Figure 2**a and b). Note that we consider here that no water or cations species are intercalated within the sheets. In Figure 2 c and d, the corresponding elastic modulus determined from the graph gave comparable values ranging from 12 to 75 GPa in air, and from 7 to 70 GPa in water. The fact that the elastic moduli found in air and in water are comparable

demonstrates that the approach developed here is reliable for the quantification. The broad distribution of the CR frequencies is due to *i*) the high surface roughness (~500 nm) that leads to changes in the contact radius between the tip and the sample's surface as it is scanned across the surface, *ii*) the presence of defects in the 2D sheets that contribute to inhomogeneity in the local stiffness,[47] and/or *iii*) different moieties of the Ti_3C_2 surfaces. Therefore, we predicted the Young's modulus of multilayer AB stacked $Ti_3C_2T_x$ using density functional theory (DFT) simulations for F, O, and OH-terminated sheets (see Figure 2c and Supplementary Information 5 for details). Clearly, the surface terminations have a significant impact on the elasticity because they directly contribute to the electrostatic interactions between the sheets through van der Waals and hydrogen bonds. The gap distance (*D*) between two MXene layers was only 0.57 Å for OH terminations, much narrower than ~ 2.5 Å for O and F terminations, due to the formation of hydrogen bonds between OH groups, resulting in a higher $E_\perp$. The surface chemistry of MXenes significantly contributes to the large scattering of CR frequencies observed in the experiments. It has been reported that hydroxyl groups and fluorine are dominant on the MXene surface.[48,49] However, due to the complexity of the surface terminations, we used $Ti_3C_2(OH)_2$ as the model system for the subsequent simulations, where the calculated $E_\perp$ for OH-terminated Ti_3C_2 can be viewed as the upper bound for experiments.

2.2. Elastic changes during Li^+ and K^+ ions intercalation

The interest in studying the mechanical changes occurring in $Ti_3C_2T_x$ comes from its large lattice shrinkage when Li^+, Na^+, or Mg^{2+} cations are intercalated along with water molecules.[33] Additionally, the actuation behavior depends on the ionic radius and charge, since the 2D structure expands when large K^+ cations are intercalated. The CR frequency images were monitored during Li^+ electrochemical intercalation/extraction at different potentials after pre-

cycling for 12 hours (5 mV s^{-1} between -0.2 V and -0.8 V vs Pt) to reach a steady state with reversible electrochemistry. As expected, the MXene paper electrode exhibited shrinkage as large as 10% after Li^+ intercalation, (**Figure 3**a). The CR frequency images were collected at different potentials in the same area of the MXene surface (Supplementary Information 6). The open circuit potential (OCP) was -0.2 V *vs* Pt reference, and most CR frequency values were between 99 and 108 kHz throughout the whole area (Figure 3b), corresponding to low modulus values ranging from 3 to 12 GPa (Figure 3c). After Li^+ intercalation the shift in the CR frequency towards larger values evidences a stiffer 2D structure, and most of the $E_\perp$ ranged between 5 and 18 GPa (Figure 3b and 3c). The narrower modulus distribution after cycling compared to the unreacted sample in Figure 2 suggests that the initial surface chemistries were modified and homogenized by the repeated faradic reactions with Li^+ ions after extensive continuous charge/discharge cycles.[50] The CR frequency images were converted to elastic modulus images that provide a more detailed picture of the electrochemical process (Figure 3 e-k). First, the overall elasticity increased with the Li^+ content during intercalation (Figure 3 e-h). While the changes were small at low overpotentials, they became noticeable at -0.6V *vs* Pt and below. The increase in $E_\perp$ is associated with a stiffening of the MXene in the normal-to-the-plane direction in the presence of Li^+ ions, and is consistent with the decrease in the inter-layer distance in this potential window.[33] Noticeably, the $E_\perp$ remained high at -0.6V during Li^+ extraction (Figure 3i). This can either indicate an ionic rearrangement between the 2D layers, or a distortion of the MXene structure associated with the redox reactions. Another explanation can be that Li^+ ions diffuse within the particle before being extracted at higher oxidative overpotentials. We refer to these ions and being in “deep” intercalation sites as opposed to “accessible” sites.[34] Finally, after full extraction of Li^+ ions (Figure 3j and 3k) the $E_\perp$ distribution was the same as

that of the original state in Figure 3e. This means that *i*) the tip shape remained unchanged during the multiple scans, therefore the changes are fundamentally associated with the elasticity of the MXene material, *ii*) despite the large variation in the volume and elastic properties, the reversible behavior of the MXene deformation demonstrates excellent mechanical recovery, and *iii*) the changes in elastic modulus are unambiguously related to ion intercalation.

Therefore, the results provide a clear visualization of the charge storage process within small areas and with high resolution. Upon application of negative potentials, the increase in the $E_{\perp}$ values first occurs at the accessible sites of the MXene flake. Only at high overpotential the $E_{\perp}$ increases significantly at the deep sites of the particle and finally, the particle appears more homogeneous (Figure 3h). The interesting feature here is that the intercalation path can be visualized, as it forms channels that "feed" the central part of the flake (see arrows in Figure 3h). It also demonstrates the difference in the cation accessibility between easily accessible and deep sites of the 2D particle, as it was suggested elsewhere.[34]

The CR AFM sensitivity to the nature of the cation was demonstrated by performing the same experiment in 0.5 M K_2SO_4 electrolyte. When K^+ ions were intercalated, the $Ti_3C_2T_x$ exhibited very little volume changes compared to Li^+ (**Figure 4**a), that may lead to different elasticity changes between both cases. Although the measurements showed an increase of the contact stiffness, it appeared significantly lower than in the case of Li^+ ions (Figure 4b and 4c). Importantly, very little changes were observed in the center of the few-layers flake (Figure 4d-k). Clearly in this case, most changes occurred at the edges of the MXene flake even at high negative overpotentials.

To better understand and quantify the changes in the mechanical properties, we subtracted the $E_{\perp}$ values from the images at fully charged and discharged states (h and k in Figure 3 and 4), to

obtain the maximum variation throughout the selected areas. As a result, **Figure 5**a enables easy identification of the accessible and deep intercalation sites (pointed with red and white arrows, respectively). The variations imaged for Li^+ in Figure 5a and K^+ in Figure 5b contrasts drastically, since very few changes can be evidenced. A major advantage of the CR AFM monitoring is that the $E_\perp$ values can be selectively extracted from the image at specific regions of interest. As discussed above, the cation intercalation in the MXene compound is not homogeneous and some sites accommodate the cations before their less accessible counterparts. The $E_\perp$ values were extracted in the same respective regions at different potentials for both Li^+ and K^+ (Figure 5c and 5d). Surprisingly, some sites exhibited a change of more than 15 GPa between fully charged and discharged states in the case of Li^+ intercalation. In contrast, the largest changes were in the order of few GPa for K^+ intercalation. This observation is consistent with the macroscopic deformation measured by dilatometry experiments that evidenced a large contraction upon Li^+ intercalation, and little volume change for K^+ intercalation.[33]

2.3. Theoretical calculations

To obtain more physical insight on those change, we used DFT to calculate the elastic modulus of $Ti_3C_2(OH)_2$ with various intercalated species and contents. Table 1 shows the DFT results of $E_\perp$ and the gap distance D between two MXene layers as a function of the water molecules contents (technical details and the full list of calculations are shown in Supplementary Information 7). The DFT calculations agreed well with experiments since the presence of only 12.5% H_2O resulted in a dramatic decrease of $E_\perp$ from 126 GPa of the dry sample to 29 GPa. The gap between the MXene layers increased from 0.57 Å to 3.51 Å, a distance sufficiently large to break the hydrogen bonds between MXene sheets, and to create sufficient space to accommodate the external stress, thereby producing a soft structure with low elasticity. On

increasing the water content to 50%, the elastic modulus reached a minimum around 18 GPa and the gap distance increased to 4.34 Å. In this case, a single water layer is formed, and the attractive forces between MXene sheets are fully compensated. Higher water contents resulted in larger $E_{\perp}$ values, possibly due to the formation of a second water layer. Although the true amount of water in MXenes remains unknown, judging from the elastic modulus and *c* lattice constants previously measured by X-ray,[33] we can conclude that there is no more than 50% H_2O in the 2D channels of $Ti_3C_2(OH)_2$.

Similar to the water intercalation, we calculated the modulus of $Ti_3C_2(OH)_2$ at different cation contents with 25% water present, since this gave the best match with the experimentally measured *c* lattice parameters. Although the DFT results (Table 2) were slightly larger than the experimental ones, they confirmed the significant increase of the modulus in the presence of Li^+ ions. Based on the present calculations, it seems that the intercalated cation pushes out one hydrogen atom from the surface hydroxyl group, forming strong bonds with oxygen atoms that enhance the stiffness of the cation/water/MXene system (Supplementary Information 8). At high K^+ contents, the DFT calculations predicted an increase in the elastic modulus of $Ti_3C_2(OH)_2$, which was not measured experimentally. Although this is not understood yet, we can reasonably assume that this discrepancy is related to the changing amount of water between the sheets as the cations are intercalated. Dynamic studies have already showed that water molecules are expelled from the 2D structure during cation intercalation due to the overcrowding effect,[33] suggesting a combined effect of cation penetration and water expulsion on the mechanical properties. Furthermore, the DFT calculations carried out on a perfect $Ti_3C_2(OH)_2$ unit cell consider neither the presence of defects, nor other surface terminations such as O or F, nor the applied electric

field. All of these factors may account for the difference between the experimental and theoretical values.

3. Conclusions

The results reported here have important implications for understanding the charge storage processes in intercalation compounds and provide a new path for studying the mechanical evolution of energy materials. For the first time, we showed that the stiffness of the material in the direction normal to the basal plane can be more than doubled upon Li^+ intercalation in presence of water. Experiments in Li_2SO_4 and K_2SO_4 electrolytes revealed that changes in the elastic modulus can be controlled with a proper electrolyte/electrode combination. Via elastic measurements, the cations intercalation pathways were tracked locally and the electrode/electrolyte couple was efficiently interpreted. Mapping the elasticity as a function of the cation content provides evidence of the spatial distribution for cation intercalation within particle with complex geometry. The CR AFM technique, together with DFT calculations, indicates directions towards a better control of the electrode/electrolyte interface by probing the mechanical properties associated with the cation storage. However, many questions remain for a better comprehension of the storage mechanism in MXene, in particular regarding the role of water molecules. Although steric expulsion of water molecules from the structure slits certainly contributes to the stiffening, their arrangement in the 2D structure is still not understood. It can also contribute to the stiffening via the formation of highly ordered water layers between the sheets, like it was recently evidenced for hydroxylated graphene.[9] Since the ionic transport in the 2D layers is strongly associated with the water content, characterizing the water structure is critical to understand the elastic behavior and further improve the electrode performance. AFM

techniques are very suitable for characterizing elastic properties with high spatial resolution in liquids, and can be further improved by imaging the viscous losses in order to obtain a full spectrum of mechanical properties. Additionally, developing scanning probe microscopy techniques with improved time resolution will be a step towards dynamic characterizations.

4. Experimental Section

MXene material: $Ti_3C_2T_x$ was synthesized by etching Al from Ti_3AlC_2 using 48% concentrated hydrofluoric acid (HF) at room temperature (RT) for 18 h as described in reference [51]. After washing to remove the etching products followed by drying, $Ti_3C_2T_x$ powder was intercalated by dimethylsulfoxide (DMSO). Then, the intercalated MXene powder was sonicated in deionized water and centrifuged. The resulted colloidal solution of delaminated MXene was vacuum-filtered to produce free-standing MXene "paper".[32] The latter, consisting of parallel oriented flakes (SI 1), was used directly as the working electrode (thickness of 2 μm).

Contact resonance AFM measurements: CR measurements were conducted on a Cypher AFM (Oxford Instruments, UK) in air and liquid environments using the Band Excitation (BE) approach during scanning in contact mode.[43] A 120 kHz large frequency excitation band was sent to the cantilever by a photothermal laser at the base of the cantilever. The cantilever response was detected and then Fourier transformed to extract the contact resonance peak. The contact resonance frequency was extracted from each contact resonance curve via fitting using a Simple Harmonic Oscillator (SHO) model. Tip calibrations were conducted in air and in 18 MΩ deionized water on reference samples (freshly cleaved HOPG and Fused silica obtained from Brucker, Germany). The respective Young's moduli were 18 GPa for HOPG and 72.9 GPa for fused silica. The tip used in this study was an Au-coated Silicon probe (PPPFM-Au,

Nanosensors, USA) with a spring constant $k_c \sim 2$ N/m and a free resonance frequency in air $f_0 \sim 55$ kHz. Typical parameters for the cantilever employed were: $L = 125$ μm, $L_1 = 115$ μm, $h = 12$ μm, and angle = 12 °. The tip was calibrated before and after the measurements to ensure that the tip itself has not changed during the measurement. While scanning, the applied normal force on the sample was set sufficiently low at 45 nN so a spherical type contact could be assumed. Additionally the low normal force enabled accurate measurements at the surface-near region, sensitive to the top few-layers.

All measurements were performed in the same area. In order to improve the local analysis, small drifts in x and y were calculated based on the topography images and the images were corrected and smoothed in order to avoid analysis artifacts due to the presence of strong pixel to pixel signal changes.

Electrochemical measurements: An electrochemical cell was attached to the scanner and was constituted of an activated carbon counter electrode, a Pt wire quasi-reference electrode (-0.2V *vs* Ag/AgCl) and a 3×3 mm^2 MXene paper working electrode facing up for an easy access of the AFM tip to its surface. The cell was connected to a potentiostat (VSP 200, Biologic S.A., France) for controlling the state of charge of the MXene. In all experiments the AFM scan rate was kept constant at 1μm/s. The in-situ experiments were performed in 1M Li_2SO_4 and 0.5M K_2SO_4 electrolytes (Sigma Aldrich, USA). Between the scans, the potential of the MXene electrode was swept at a rate of 2 mV/s and hold until the current reached a constant value, typically after 20 minutes. Before the CR AFM measurements, the MXene paper was cycled for 12 hours to ensure maximum access of cations to the intercalation sites and reach full capacitance.

Density Functional Theory simulations: First-principles calculations were carried out using density functional theory (DFT) [52] and the all-electron projector augmented wave method [53] as implemented in the Vienna ab initio simulation package.[54] The Van der Waals density functional of optB86b was considered for all simulations.[55] A plane-wave cutoff energy of 580 eV was sufficient to ensure convergence of the total energies to 1 meV per primitive cell. Structural optimizations used a convergence criterion of 10^{-5} eV/cell in energy and 0.05 eV/Å in force. The MXene sheets were arranged in a AB stacking geometry. The intercalations were studied on 2 × 1 × 1 and/or 2 × 2 × 1 supercells in orthorhombic lattices with 4 × 4 × 1 gamma-centered Brillouin zone sampling.[56] To simplify the simulation, the inserted cations were treated as neutral atoms. The Young's modulus was predicted from the elasticity stiffness tensors, which were calculated using strain-stress approach. For transversely isotropic materials, we used the 5 independent elastic constants: C_{11}, C_{12}, C_{13}, C_{33}, and C_{44}. Then the elastic constants were calculated by:

$$E_{\perp} = E_z = C_{33} - 2\,C_{13}\,C_{13}/(\,C_{11} + C_{12}) \quad (3)$$

Supporting Information

Supporting Information is available from the Wiley Online Library or from the author.

Acknowledgements

The experiments and sample preparation in this work were supported as part of the Fluid Interface Reactions, Structures and Transport (FIRST) Center, an Energy Frontier Research Center funded by the U.S. Department of Energy, Office of Science, Office of Basic Energy Sciences. The facilities to perform the experiments were provided by the Center for Nanophase Materials Sciences, which is a DOE Office of Science user facility. This research used resources of the National Energy Research Scientific Computing Center, a DOE Office of Science User

Facility supported by the Office of Science of the U.S. Department of Energy under Contract No. DE-AC02-05CH11231.

References

[1] C. Poellmann, P. Steinleitner, U. Leierseder, P. Nagler, G. Plechinger, M. Porer, R. Bratschitsch, C. Schuller, T. Korn, R. Huber, *Nat Mater* **2015** *14*, 889.
[2] K. A. Lin, A. Jenkins, J. P. Valdes-Garcia, D. B. Small, P. Farmer, Avouris, *Nano Lett.* **2009** *9*, 422.
[3] X. Yang, C. Cheng, Y. Wang, L. Qiu, D. Li, *Science* **2013** *341*, 534.
[4] C. Lee, Q. Li, W. Kalb, X.-Z. Liu, H. Berger, R. W. Carpick, J. Hone, *Science* **2010** *328*, 76.
[5] S. Kim, S. Zhou, Y. Hu, M. Acik, Y. J. Chabal, C. Berger, W. de Heer, A. Bongiorno, E. Riedo, *Nat Mater* **2012** *11*, 544.
[6] L. Ci, L. Song, C. Jin, D. Jariwala, D. Wu, Y. Li, A. Srivastava, Z. F. Wang, K. Storr, L. Balicas, F. Liu, P. M. Ajayan, *Nat Mater* **2010** *9*, 430.
[7] C. Lee, X. Wei, J. W. Kysar, J. Hone, *Science* **2008** *321*, 385.
[8] K. H. Michel, B. Verberck, *Physica Status Solidi (b)* **2008** *245*, 2177.
[9] Y. Gao, S. Kim, S. Zhou, H.-C. Chiu, D. Nelias, C. Berger, W. de Heer, L. Polloni, R. Sordan, A. Bongiorno, E. Riedo, *Nat Mater* **2015** *14*, 714.
[10] H. Wagner, D. Bedorf, S. Küchemann, M. Schwabe, B. Zhang, W. Arnold, K. Samwer, *Nat Mater* **2011** *10*, 439.
[11] N. Shpigel, M. D. Levi, S. Sigalov, O. Girshevitz, D. Aurbach, L. Daikhin, N. Jackel, V. Presser, *Angew Chem Int Ed Engl* **2015** *54*, 12353.
[12] M. M. Hantel, T. Kaspar, R. Nesper, A. Wokaun, R. Kotz, *Electrochem. Commun.* **2011** *13*, 90.
[13] T. M. Arruda, M. Heon, V. Presser, P. C. Hillesheim, S. Dai, Y. Gogotsi, S. V. Kalinin, N. Balke, *Energ. Environ. Sci.* **2013** *6*, 225.
[14] M. M. Hantel, V. Presser, R. Kotz, Y. Gogotsi, *Electrochem. Commun.* **2011** *13*, 1221.
[15] M. M. Hantel, D. Weingarth, R. Kötz, *Carbon* **2014** *69*, 275.
[16] N. Balke, S. Jesse, Y. Kim, L. Adamczyk, A. Tselev, I. N. Ivanov, N. J. Dudney, S. V. Kalinin, *Nano Lett* **2010** *10*, 3420.
[17] M. Naguib, O. Mashtalir, J. Carle, V. Presser, J. Lu, L. Hultman, Y. Gogotsi, M. W. Barsoum, *ACS Nano* **2012** *6*, 1322.
[18] M. Naguib, M. Kurtoglu, V. Presser, J. Lu, J. Niu, M. Heon, L. Hultman, Y. Gogotsi, M. W. Barsoum, *Adv. Mater.* **2011** *23*, 4248.
[19] M. Naguib, Y. Gogotsi, *Acc Chem Res* **2015** *48*, 128.
[20] M. Ghidiu, M. Naguib, C. Shi, O. Mashtalir, L. M. Pan, B. Zhang, J. Yang, Y. Gogotsi, S. J. Billinge, M. W. Barsoum, *Chem. Commun.* **2014** *50*, 9517.
[21] M. Naguib, V. N. Mochalin, M. W. Barsoum, Y. Gogotsi, *Adv. Mater.* **2014** *26*, 992.
[22] Y. Lee, Y. Hwang, Y.-C. Chung, *ACS Appl. Mater. Interfaces* **2015** *7*, 7163.
[23] X.-f. Yu, J.-b. Cheng, Z.-b. Liu, Q.-z. Li, W.-z. Li, X. Yang, B. Xiao, *R. Soc. Chem. Adv.* **2015** *5*, 30438.
[24] Z. Lin, D. Sun, Q. Huang, J. Yang, M. W. Barsoum, X. Yan, *J. Mater. Chem. A* **2015** *3*, 14096.
[25] C. Xu, L. Wang, Z. Liu, L. Chen, J. Guo, N. Kang, X. L. Ma, H. M. Cheng, W. Ren, *Nat Mater* **2015** *14*, 1135.
[26] M. Kurtoglu, M. Naguib, Y. Gogotsi, M. W. Barsoum, *MRS Communications* **2012** *2*, 133.
[27] V. N. Borysiuk, V. N. Mochalin, Y. Gogotsi, *Nanotechnology* **2015** *26*, 265705.

[28] M. Naguib, J. Come, B. Dyatkin, V. Presser, P. L. Taberna, P. Simon, M. W. Barsoum, Y. Gogotsi, *Electrochem. Commun.* **2012** *16*, 61.
[29] J. Come, M. Naguib, P. Rozier, M. W. Barsoum, Y. Gogotsi, P. L. Taberna, M. Morcrette, P. Simon, *J. Electrochem. Soc.* **2012** *159*, A1368.
[30] M. Ghidiu, M. R. Lukatskaya, M. Q. Zhao, Y. Gogotsi, M. W. Barsoum, *Nature* **2014** *516*, 78.
[31] M. R. Lukatskaya, S. M. Bak, X. Q. Yu, X. Q. Yang, M. W. Barsoum, Y. Gogotsi, *Adv. Energy Mater.* **2015** *5*, 1500589.
[32] M. R. Lukatskaya, O. Mashtalir, C. E. Ren, Y. Dall'Agnese, P. Rozier, P. L. Taberna, M. Naguib, P. Simon, M. W. Barsoum, Y. Gogotsi, *Science* **2013** *341*, 1502.
[33] J. Come, J. M. Black, M. R. Lukatskaya, M. Naguib, M. Beidaghi, A. J. Rondinone, S. V. Kalinin, D. J. Wesolowski, Y. Gogotsi, N. Balke, *Nano Energy* **2015** *17*, 27.
[34] M. D. Levi, M. R. Lukatskaya, S. Sigalov, M. Beidaghi, N. Shpigel, L. Daikhin, D. Aurbach, M. W. Barsoum, Y. Gogotsi, *Adv. Energy Mater.* **2015** *5*, 1400815.
[35] D. G. Yablon, A. Gannepalli, R. Proksch, J. Killgore, D. C. Hurley, J. Grabowski, A. H. Tsou, *Macromolecules* **2012** *45*, 4363.
[36] A. Gannepalli, D. G. Yablon, A. H. Tsou, R. Proksch, *Nanotechnology* **2011** *22*, 355705.
[37] U. Rabe, V. Scherer, S. Hirsekorn, W. Arnold, *Journal of Vacuum Science & Technology B* **1997** *15*, 1506.
[38] U. Rabe, S. Amelio, M. Kopycinska, S. Hirsekorn, M. Kempf, M. Göken, W. Arnold, *Surf. Interface Anal.* **2002** *33*, 65.
[39] G. Stan, S. Krylyuk, A. V. Davydov, M. D. Vaudin, L. A. Bendersky, R. F. Cook, *Ultramicroscopy* **2009** *109*, 929.
[40] Q. Li, S. Jesse, A. Tselev, L. Collins, P. Yu, I. Kravchenko, S. V. Kalinin, N. Balke, *ACS Nano* **2015** *9*, 1848.
[41] A. Labuda, J. Cleveland, N. A. Geisse, M. Kocun, B. Ohler, R. Proksch, M. B. Viani, D. Walters, *Microscopy and analysis* **2014** *28*, S21.
[42] M. Kocun, A. Labuda, A. Gannepalli, R. Proksch, *Rev Sci Instrum* **2015** *86*, 083706.
[43] S. Jesse, S. V. Kalinin, R. Proksch, A. P. Baddorf, B. J. Rodriguez, *Nanotechnology* **2007** *18*, 435503.
[44] U. Rabe, S. Amelio, E. Kester, V. Scherer, S. Hirsekorn, W. Arnold, *Ultrasonics* **2000** *38*, 430.
[45] Z. Parlak, Q. Tu, S. Zauscher, *Nanotechnology* **2014** *25*, 445703.
[46] R. C. Tung, J. P. Killgore, D. C. Hurley, *J. Appl. Phys.* **2014** *115*, 224904.
[47] J. Halim, K. M. Cook, M. Naguib, P. Eklund, Y. Gogotsi, J. Rosen, M. W. Barsoum, *Appl. Surf. Sci.* **2015**, in press.
[48] Y. Xie, M. Naguib, V. N. Mochalin, M. W. Barsoum, Y. Gogotsi, X. Yu, K. W. Nam, X. Q. Yang, A. I. Kolesnikov, P. R. Kent, *J. Am. Chem. Soc.* **2014** *136*, 6385.
[49] H.-W. Wang, M. Naguib, K. Page, D. J. Wesolowski, Y. Gogotsi, *Chem. Mater.* **2016** *28*, 349.
[50] Y. Dall'Agnese, M. R. Lukatskaya, K. M. Cook, P. L. Taberna, Y. Gogotsi, P. Simon, *Electrochem. Commun.* **2014** *48*, 118.
[51] O. Mashtalir, M. Naguib, B. Dyatkin, Y. Gogotsi, M. W. Barsoum, *Mater. Chem. Phys.* **2013** *139*, 147.
[52] W. Kohn, L. J. Sham, *Physical Review* **1965** *140*, A1133.
[53] P. E. Blöchl, *Phys. Rev. B* **1994** *50*, 17953.

[54] G. Kresse, J. Furthmüller, *Phys. Rev. B* **1996** *54*, 11169.
[55] J. Klimeš, D. R. Bowler, A. Michaelides, *Phys. Rev. B* **2011** *83*, 195131.
[56] H. J. Monkhorst, J. D. Pack, *Phys. Rev. B* **1976** *13*, 5188.

Figures

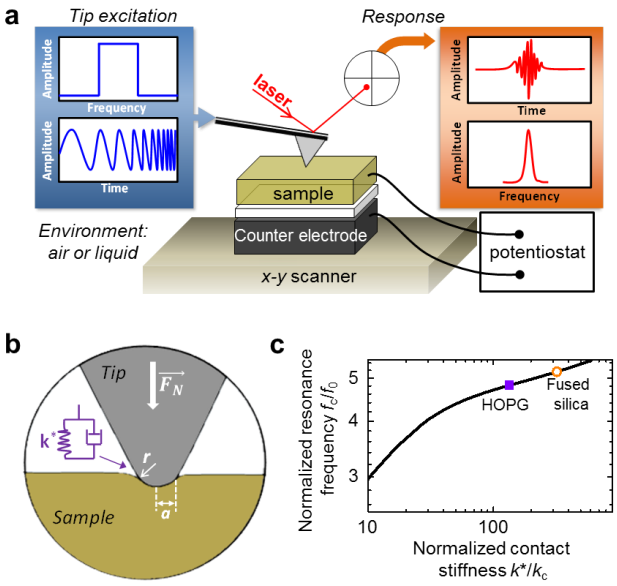

Figure 1. In situ contact resonance AFM measurements during electrochemical cycling. a) schematic representation of the experimental setup, where the AFM tip is vibrated in contact with the sample's surface with a band excitation waveform. b) schematic representation of the tip-sample contact model, where the tip indenter forms a contact radius *a* with the sample's surface. c) calculated calibration curve in water for AFM cantilever used in this study (see Supplementary Information 2 for more details).

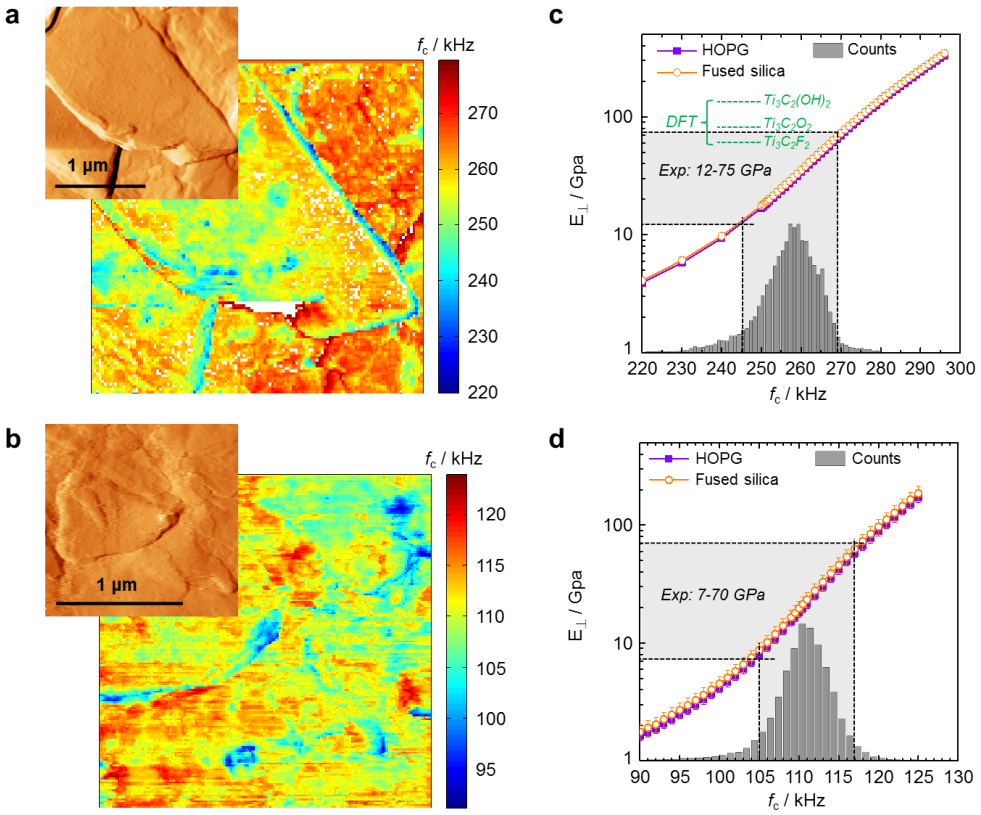

Figure 2. Contact resonance AFM images of the unreacted $Ti_3C_2T_x$ electrode. CR AFM images a) in air and b) in water, together with corresponding topography images. c), d) calibration curves with error bars obtained from HOPG and fused silica reference samples c) in air and d) water, together with the experimental counts of CR frequencies for the MXene electrode paper in air and water. A spherical indenter (m=1.5) was considered.

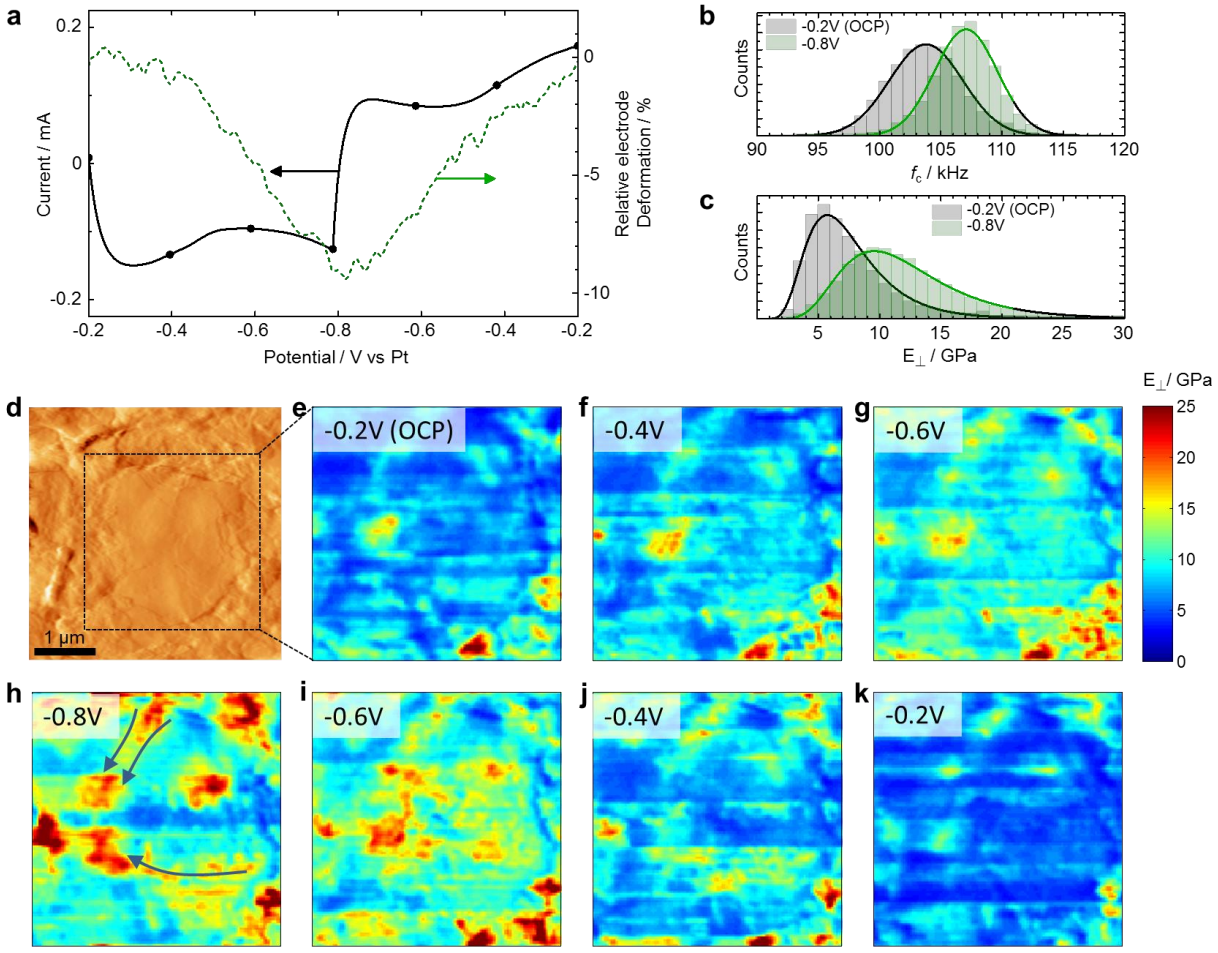

Figure 3. Elastic changes of $Ti_3C_2T_x$ in Li_2SO_4 electrolyte. a) electrochemical profile of Li^+ intercalation/extraction showing the current and single point relative electrode deformation profiles as a function of potential. b) contact resonance frequency distribution histograms at discharged and discharged states. c) corresponding elastic modulus distribution histograms. d) contact AFM topography image of a multilayer MXene flake at the surface of the electrode. e-k) elastic modulus images taken at potentials between -0.2 V and -0.8 V vs Pt during Li^+ charge (e-h) and discharge (h-k).

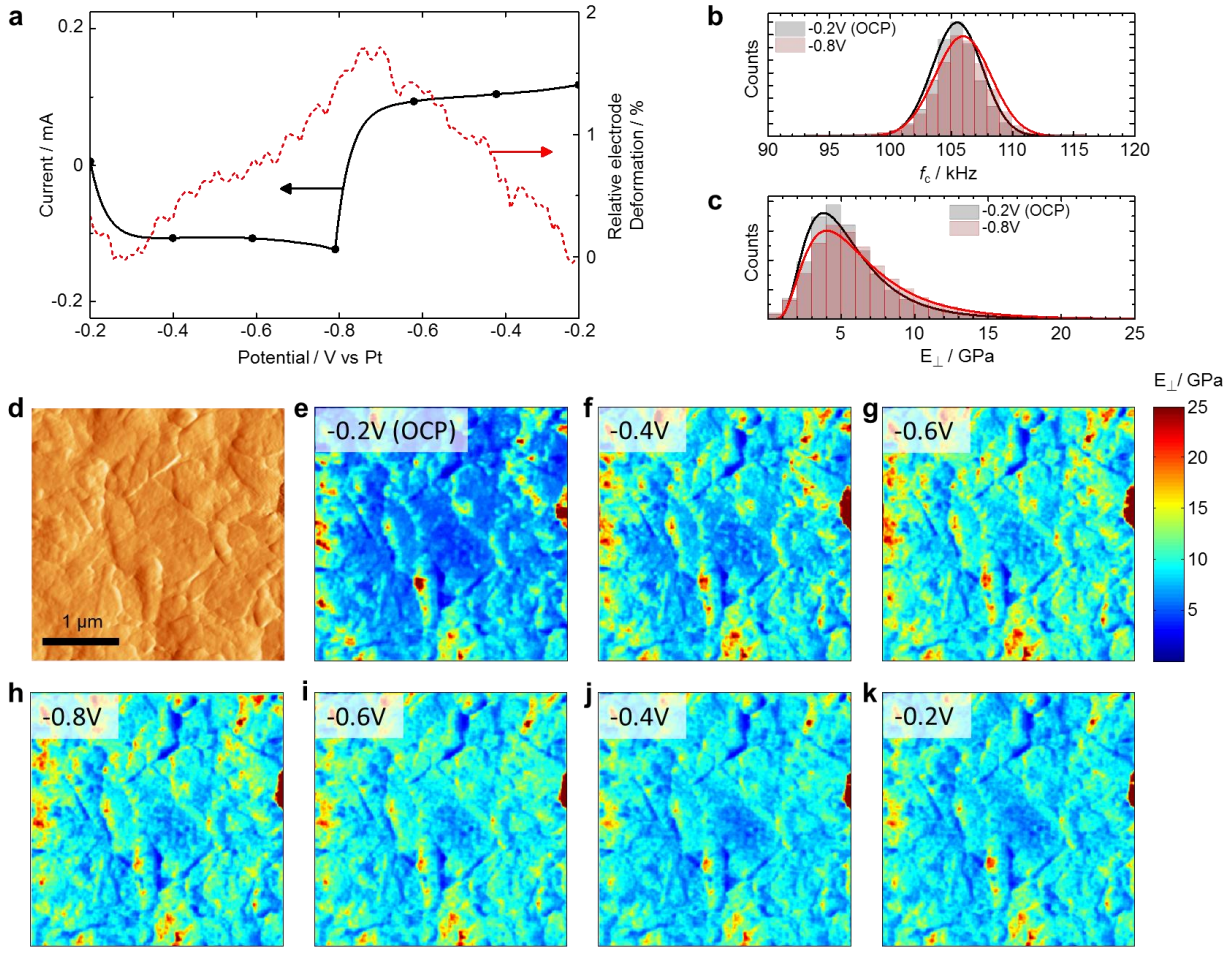

Figure 4. Elastic changes of $Ti_3C_2T_x$ in K_2SO_4 electrolyte. a) electrochemical profile of K^+ intercalation/extraction showing the current and single point relative electrode deformation profiles as a function of potential. b) contact resonance frequency distribution histograms at discharged and discharged states. c) corresponding elastic modulus distribution histograms. d) contact AFM topography image of a multilayer MXene flake at the surface of the electrode. e-k) elastic modulus images taken at potentials between -0.2 V and -0.8 V vs Pt during K^+ charge (e-h) and discharge (h-k).

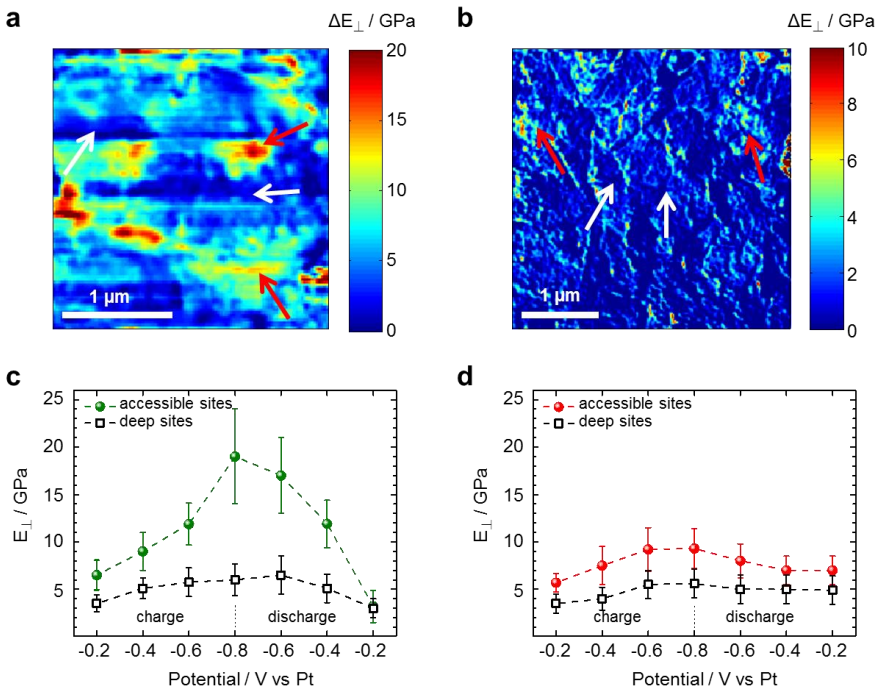

Figure 5. Evolution of elastic modulus at different cation contents for accessible and deep intercalation sites. Maximum elastic modulus difference between charged and discharged states for a) Li^+ and b) K^+. Red and white arrows point accessible and deep sites, respectively. Elastic modulus values as a function of electrode potential during charge and discharge in c) 1 M Li_2SO_4 and d) 0.5 M K_2SO_4 electrolytes.

Table 1. Calculated elastic modulus, gap distance D, and *c* lattice parameter of $Ti_3C_2(OH)_2$ as a function of intercalated water content.

H_2O [%]	$E_\perp$ [GPa]	D [Å]	*c* [Å]
12.5	29	3.51	25.45
25	28	3.64	25.69
50	18	4.34	27.05
75	49	6.24	30.85
100	55	6.64	31.58

Table 2. Elastic modulus of multilayer $Ti_3C_2(OH)_2$ calculated by DFT compared with values obtained experimentally.

	$E_{\perp}$ [GPa] (testing or calculations conditions)			
Measured by CR AFM	12-75 (dry $Ti_3C_2T_x$)	2-12 (in water)	5-18 (Cycled in aqueous Li_2SO_4)	3-13 (Cycled in aqueous K_2SO_4)
DFT calculated	125 (dry $Ti_3C_2(OH)_2$)	28 (25% H_2O, $Ti_3C_2(OH)_2$)	48 (25% H_2O, $Ti_3C_2(OH)_2Li_{0.25}$)	46 (25% H_2O, $Ti_3C_2(OH)_2K_{0.25}$)